DISSERTAÇÃO DE MESTRADO

INFLUENCE OF SMALL DEFECTS ON THE FATIGUE LIMIT OF 304L STAINLESS STEEL: AXIAL-TORSIONAL EXPERIMENTS AND MODELING

ARTUR LOPES DIAS

Brasília, 06 de março de 2020

UNIVERSIDADE DE BRASÍLIA

FACULDADE DE TECNOLOGIA
DEPARTAMENTO DE ENGENHARIA MECÂNICA

UNIVERSIDADE DE BRASÍLIA

Faculdade de Tecnologia
Departamento de Engenharia Mecânica

INFLUENCE OF SMALL DEFECTS ON THE FATIGUE LIMIT OF 304L STAINLESS STEEL: AXIAL-TORSIONAL EXPERIMENTS AND MODELING

ARTUR LOPES DIAS

DISSERTAÇÃO DE MESTRADO SUBMETIDA AO DEPARTAMENTO DE ENGENHARIA MECÂNICA DA FACULDADE DE TECNOLOGIA DA UNIVERSIDADE DE BRASÍLIA, COMO PARTE DOS REQUISITOS NECESSÁRIOS PARA A OBTENÇÃO DO GRAU DE MESTRE EM CIÊNCIAS MECÂNICAS.

APROVADA POR:

_____

Prof. Fábio Comes de Castro, D.Sc. (ENM/UnB)
(Orientador)

_____

Prof. Jorge Luiz de Almeida Ferreira, D.Sc. (ENM/UnB)
(Examinador Interno)

_____

Prof. Luís Augusto Conte Mendes Veloso, D.Sc. (ENM/UnB)
(Examinador Externo)

Brasília/DF, 06 de março de 2020.

FICHA CATALOGRÁFICA

DIAS, ARTUR LOPES

Influence of small defects on the fatigue limit of 304L stainless steel: axial-torsional experiments and modeling

[Distrito Federal] 2020.

xi, 33 p., 210 x 297 mm (ENM/FT/UnB, Mestre, Ciências Mecânicas, 2020)

Dissertação de mestrado – Universidade de Brasília.

Faculdade de Tecnologia.

Departamento de Engenharia Mecânica.

1. Fatigue limit
2. Defects
3. 304L stainless steel
4. $\sqrt{area}$ parameter model

I. ENM/FT/UnB

II. ENM.DM-__/2020

REFERÊNCIA BIBLIOGRÁFICA

DIAS, A. L., (2020) Influence of small defects on the fatigue limit of 304L stainless steel: axial-torsional experiments and modeling. Dissertação de mestrado, Publicação ENM.DM-__/2020, Departamento de Engenharia Mecânica, Universidade de Brasília, DF, 33 p.

CESSÃO DE DIREITOS

AUTOR: Artur Lopes Dias.

TÍTULO: Influence of small defects on the fatigue limit of 304L stainless steel: axial-torsional experiments and modeling.

GRAU: Mestre ANO: 2020

Artur Lopes Dias
EPTG QE 4, bloco B-3, Ed. Rio Tapajós. Apto. 206
71100168 Lúcio Costa-Guará, Brasília – DF – Brasil.

Agradecimentos

Primeiramente agradeço a minha esposa, Jéssica Amazonas, pela paciência e compreensão que teve em todo esse tempo de estudo. Agradeço aos meus familiares que sempre me apoiaram, principalmente a minha mãe, Vilma Lopes, que lutou para sustentar e manter a nossa família. Agradeço também aos familiares da minha esposa, principalmente aos meus sogros, que sempre nos apoiam.

Agradeço ao meu orientador Professor Fábio Castro pela grande dedicação ao seu trabalho e excelente orientação aos seus alunos. Agradeço aos professores Jorge Luiz Ferreira, Luís Veloso, Edgar Mamiya, José Alexander, Thiago Doca, Aline de Paula, Lucival Malcher, e a todos os outros professores em que pude ter algum contato nesses dois anos de estudo e que de alguma forma me auxiliaram, seja por meio de uma disciplina ou apenas por algum comentário construtivo.

Sou grato aos técnicos colaboradores Adriano Lopes, Wesley Valadares, Rafael Barros, Ivan Reis, Ricardo Rodrigues e Edson de Almeida pelo fundamental suporte no uso dos equipamentos. Agradeço ao Sr. Reginaldo e à Sra. Raimunda pelo serviço prestado na portaria do SG9, ao Rafael Queiros e ao Bruno Martins pelos serviços realizados na secretaria e a toda equipe de limpeza do prédio SG9 pelo ótimo trabalho.

Agradeço aos meus amigos de estudo e pesquisa, Daniel Oliveira, Ian Matos, Vinicius Rodrigues, Natalia Torres, Gustavo Heinke, Thiago Primo, Maycol Coutinho, Lucas Carneiro, Erick Vieira, Sarah Souza, Leonel Morales, Roberto Costa, Guilherme Ferreira, Felipe Canut e principalmente ao Cainã Bemfica, pelo amplo auxílio e apoio. Agradeço a todos os outros alunos pelas conversas, conselhos e momentos de descontração. Agradeço também ao Matheus Elias que apesar de não ter continuado conosco no programa nos deu grande auxílio na usinagem dos corpos de prova.

Não poderia deixar de agradecer a todos os meus amigos do IFB que sempre me apoiaram e auxiliaram nesses dois anos de estudo e trabalho, principalmente ao Rodrigo Abdo, Álvaro Eduardo, Leandro Pinheiro, Edinaldo Silva, Paulo César, Yuri Toledo, Erich Souza, Paulo Baltazar, Nilton Borges, Ronaldo Correia e a todos os outros professores e colaboradores do campus que de alguma forma me apoiaram. Também agradeço a todos os amigos de fora da UnB e do IFB que sempre me apoiaram.

Por fim, gostaria de agradecer a Coordenação de Aperfeiçoamento de Pessoal de Nível Superior – CAPES, que forneceu apoio financeiro para que a realização do projeto fosse possível. Agradeço também ao Instituto Federal de Brasília, Campus Estrutural, por me apoiar liberando horas para que eu pudesse participar das aulas e dos experimentos referentes a minha pesquisa na Universidade de Brasília.

Abstract

The influence of small defects on the fatigue limit of 304L stainless steel is investigated in this work. Fully reversed axial-torsional fatigue tests were carried out at room temperature on specimens containing a cylindrical defect with $\sqrt{area} = 400$ μm. The loading conditions used in the tests were: axial, torsional, in-phase, 90º out-of-phase, and square-shape. In all tests, non-propagating cracks in the vicinity of the defect were not observed after 2×10^6 cycles (run-out condition). The absence of non-propagating cracks indicates that the threshold condition for crack initiation, instead of crack propagation, determines the fatigue limit of 304L stainless steel containing the defect type investigated. Crack orientation in the vicinity of the defect was measured for the tests conducted just above the fatigue limit. A critical plane fatigue criterion for metals containing small defects, which was recently developed at the University of Brasilia, was evaluated using the new test data for 304L stainless steel. The differences between estimated and observed fatigue limits were within a range of 11 to 15% when the model was calibrated using the Murakami–Endo expression for the uniaxial fatigue strength. Calibration of the model using the experimentally measured uniaxial fatigue strength yielded fatigue limits differing -2 to 3% from the observed values. The overall good agreement between estimated and observed crack angles suggests that the cracking behavior of 304L stainless steel containing a small defect is primarily governed by normal stresses (Mode I failure).

Resumo

Este trabalho investigou a influência de pequenos defeitos no limite de fadiga do aço inoxidável 304L. Ensaios de fadiga controlados por força e/ou torque foram realizados em corpos de prova contendo um defeito cilíndrico com $\sqrt{area} = 400$ μm. As condições de carregamento investigadas foram: axial, torção, em fase, 90º fora de fase e trajetória quadrada. Em todos os ensaios, trincas não propagantes não foram observadas na vizinhança do defeito após 2×10^6 ciclos (critério de interrupção do ensaio). A ausência de trincas não propagantes indicou que a condição limiar para iniciação de uma trinca, ao invés da condição limiar para a propagação de uma trinca, determina o limite de fadiga do aço inoxidável 304L contendo o tipo de defeito estudado. Em todos os ensaios conduzidos com amplitude de carregamento logo acima do limite de fadiga, a orientação das trincas formadas na vizinhança do defeito foi medida. Um critério de fadiga baseado no conceito de plano crítico, desenvolvido recentemente na Universidade de Brasília, foi avaliado usando os novos dados experimentais do aço inoxidável 304L. A diferença entre os limites de fadiga estimados e observados ficou na faixa de 11 a 15% quando o modelo foi calibrado com a fórmula de Murakami–Endo para o limite de fadiga uniaxial. A calibração do modelo usando o limite de fadiga uniaxial medido experimentalmente resultou em estimativas com diferença de -2 a 3% dos valores observados. A boa concordância entre os ângulos estimados e observados das trincas sugere que a falha do aço inoxidável 304L contendo pequenos defeitos é governada principalmente pelas tensões normais (falha em Modo I).

Table of Contents

List of Figures

List of Tables

List of Symbols

$\sqrt{area}$	Square root of the area of a defect projected onto the plane normal to the maximum principal stress direction
FP	Fatigue parameter
H_{v}	Vickers hardness
K	Stress intensity factor
k	Stress biaxiality constant
m	Constant of the Walker relation
N	Number of cycles
N_{f}	Number of cycles to failure
t	Time
x'	x' direction of a coordinate system located at the free surface of a component
y'	y' direction of a coordinate system located at the free surface of a component
z'	z' direction of a coordinate system located at the free surface of a component
ΔK	Stress intensity factor range
ΔK_{th}	Threshold stress intensity factor range
$\Delta\sigma$	Range of the stress applied to the surface crack
θ	Orientation of the surface crack
ρ	Notch root radius
Σ	Linear combination of the normal stresses
σ	Normal stress
σ_{a}	Normal stress amplitude
$\sigma_{\mathrm{x}'}$	Normal stress in the x’ direction
$\sigma_{\mathrm{y}'}$	Normal stress in the y’ direction
σ_{w}	Uniaxial fatigue limit of a material containing a defect

$\sigma_{w'}$	Fatigue limit associated with the projection of the defect onto the plane normal to the x' direction
τ	Shear stress
τ_a	Shear stress amplitude
τ_w	Torsional fatigue limit of a material containing a defect
φ	Phase angle between axial and shear stress histories
ω	Angular frequency
$\langle\ \rangle$	Macaulay brackets

1 Introduction

1.1 Motivation

Engineering components usually contain defects such as pits, scratches and non-metallic inclusions, which can be introduced by processes such as casting, machining, and heat treatment, or by the action of the environment. It is well known that the presence of these defects may reduce the fatigue strength of metals, as indicated by numerous studies carried out over the last four decades (Murakami and Nemat-Nasser, 1983; Murakami and Endo, 1986; Murakami and Endo, 1994; Murakami, 2019).

Many studies have proposed models for predicting the fatigue limit of materials containing small defects, both for axial and multiaxial loading conditions (Murakami and Endo, 1986; Murakami and Endo, 1994; Endo, 1999; Endo and Ishimoto, 2006; Endo and Ishimoto, 2007; Endo and Yanase, 2014; Nadot and Billaudeau, 2006; Groza et al., 2018; Karolczuk et al., 2008; Murakami, 2019). However, further development of the existing models is needed. For instance, it is still unclear how to define the critical plane for irregularly shaped defects subjected to general multiaxial loading conditions.

Castro et al. (2019) developed a critical plane model for the multiaxial fatigue limit of metals containing small defects. This model was evaluated using axial-torsional test data of steels and cast irons taken from the literature (Endo, 1999; Endo and Ishimoto, 2006; Endo and Yanase, 2014; Lorenzino et al., 2015; Billaudeau, 2002; Billaudeau et al., 2004; Nadot and Billaudeau, 2006; Karolczuk, 2008), and good agreement was found between the observed and estimated fatigue limits and crack orientations. These results have encouraged the evaluation of the model using different materials and defects and more complicated loading conditions.

In the present work, an evaluation of the critical plane model proposed by Castro et al. (2019) is made using new test data of 304L stainless steel containing a small cylindrical defect. The tests were conducted under proportional and nonproportional axial-torsional loading conditions. Despite

recent efforts to understand the influence of small defects on the fatigue limit of martensitic stainless steels (Schönbauer et al., 2017b; Schönbauer et al., 2017a; Schönbauer and Mayer, 2019), studies on austenitic stainless steels are still very few (Ogura and Miyoshi, 1986; Guerchais et al., 2015). To the best of the author's knowledge, the influence of small defects (dimensions less than 1 mm) on the fatigue limit of 304L stainless steel has not previously been investigated.

1.2 Objectives

The general objectives of this work are to investigate the influence of small defects on the axial-torsional fatigue limit of 304L stainless steel and to evaluate the applicability of the critical plane fatigue criterion proposed by Castro et al. (2019) for this material. The specific objectives of this work are:

(1) To conduct force/torque-controlled fatigue tests at room temperature on 304L stainless steel containing a cylindrical small defect with $\sqrt{area} = 400$ μm. The loading conditions used in the tests were: axial, torsional, in-phase, 90º out-of-phase, and square-shape.

(2) To identify the cracking behavior of the 304L stainless steel containing a small defect by measuring the crack orientation in the vicinity of the defect.

(3) To evaluate the new critical plane fatigue criterion using the fatigue limits and crack orientations observed in the 304L stainless steel.

2 Models for the fatigue limit of metals containing small defects

Since the 1950s, methods for predicting the influence of small defects on the uniaxial fatigue strength of metals have been proposed. Murakami and Endo (1994) reviewed these methods and concluded that the $\sqrt{area}$ parameter model developed by Murakami and co-workers (Murakami and Nemat-Nasser, 1983; Murakami and Endo, 1986) has advantages over the others. For instance, the constants of the model do not need to be determined from time-consuming fatigue tests. The $\sqrt{area}$ parameter model has been successfully applied to many materials such as carbon steel, brass, and cast iron, resulting in prediction errors less than 10% in most cases (Murakami, 2019). However, the use of uniaxial models is limited by the fact that multiaxial stress states often occur in real situations due to the presence of notches and/or multiple applied loads (Beretta et al., 1997; Nadot and Denier, 2004; Giglio et al., 2010).

Endo (1999) extended the $\sqrt{area}$ parameter model to multiaxial load conditions by developing a fatigue criterion that combines the maximum and minimum principal stress amplitudes. This model was evaluated using in-phase axial-torsional test data of Cr-Mo steel (JIS SCM435), carbon steel (JIS S35C), high strength brass, and two ductile cast irons (JIS FCD400 and FCD700). The predictions were in good agreement with the experimental results. Endo's model was further improved by Endo and Ishimoto (2006) to describe the phase effect between axial and shear stress histories, and then by Endo and Ishimoto (2007) to account for the mean stress effect. Again, a good correlation between observed and estimated fatigue limits was found.

Alternative approaches to model the influence of small defects on the fatigue limit of metals have also been proposed. For instance, classical multiaxial fatigue criteria were modified by introducing a stress gradient correction term (Nadot and Billaudeau, 2006; Groza et al., 2018) or by averaging stress quantities over critical areas (Karolczuk et al., 2008). In these studies, the authors have argued in favor of conducting a three-dimensional elastic-plastic analysis to obtain the stress

distribution around the defect, which is then used as input data to a nonlocal fatigue criterion. In the work of Nadot and Billaudeau (2006), prediction errors less than 15% were reported in most cases for the axial-torsional tests conducted on three types of defects. Comparing these criteria with the $\sqrt{area}$ parameter model, the simplicity of the latter combined with its reasonably good estimates are attractive from an engineering point of view. However, even with the progress in extending the $\sqrt{area}$ parameter model to multiaxial loading conditions, further improvements are needed. For instance, it is still unclear how to define the critical plane for irregularly shaped defects subjected to general loading histories.

Based on the $\sqrt{area}$ parameter model by Murakami and Endo (1986), Castro et al. (2019) developed a critical plane criterion for the fatigue limit of metals with small defects. In this criterion, the concept of directionally dependent fatigue strength was introduced to consider defects whose projected area varies with the plane. The new criterion is well defined even when the defect is subjected to principal stress directions that vary with time. To evaluate the fatigue criterion, Castro et al. (2019) used fatigue limit data taken from the literature. First, the criterion was evaluated using the axial-torsional fatigue limit data produced by Endo and co-workers, who tested Cr-Mo steel (JIS SCM435) and carbon steel (JIS S35C) containing small surface defects, and ductile cast iron (JIS FCD400) having inherent graphite nodules (Endo, 1999; Endo and Ishimoto, 2006; Endo and Yanase, 2014). Good agreement between observed and estimated fatigue limits was found. Then, to evaluate the effect of the defect orientation on the fatigue limit, the criterion was applied to the fatigue limit data produced by Lorenzino et al. (2015). These authors tested low and medium carbon steels (JIS-S15C and JIS-S45C) containing small tilted slits under fully reversed tension-compression. The estimated critical planes and fatigue limits agreed well with the experimental observations. Lastly, the model was evaluated using the C36 steel test data obtained by Nadot and Billaudeau (Billaudeau, 2002; Billaudeau et al., 2004; Nadot and Billaudeau, 2006; Karolczuk, 2008). Hemispherical defects and hemiellipsoidal defects with different orientations, subjected to

axial-torsional loading histories (with and without mean/static stress) were studied in the evaluation. The differences between observed and estimated fatigue limits were within a range of -12 to 12% for most of the test data.

The good results provided by the new fatigue criterion has encouraged us to further evaluate it using different materials, defects, and loading conditions. In what follows, the $\sqrt{area}$ parameter model developed by Murakami and Endo (1986) for uniaxial loading conditions is summarized. Then, by taking this model as a starting point, the new fatigue criterion is described. For conciseness, only these models are reviewed in this chapter.

2.1 The $\sqrt{area}$ parameter model

This section presents an overview of the $\sqrt{area}$ parameter model proposed by Murakami and Endo for uniaxial loading conditions. In the next section, this model will serve as the basis of a multiaxial fatigue criterion for metals containing small defects.

Murakami and Endo developed a fracture mechanics-based model for estimating the effect of small defects on the fatigue limit (Murakami and Nemat-Nasser, 1983; Murakami and Endo, 1983; Murakami and Endo, 1986; Murakami, 2012; Murakami, 2019). The model is built upon experimental observations that indicate that, for various metallic materials, non-propagating cracks exist at the edge of defects at or just below the fatigue limit. Thus, the fatigue limit of a material containing a defect should be associated with the threshold condition for non-propagation of a crack initiated from the defect, and not with the threshold condition for crack initiation. The condition that characterizes the fatigue limit of defects may, therefore, be expressed as

$$\Delta K = \Delta K_{\text{th}} \tag{2.1}$$

where ΔK is the stress intensity factor range and ΔK_{th} is the threshold stress intensity factor range.

To develop a practical formula for evaluating ΔK for three-dimensional surface defects, Murakami and Endo considered an “equivalent crack” defined as the domain occupied by the

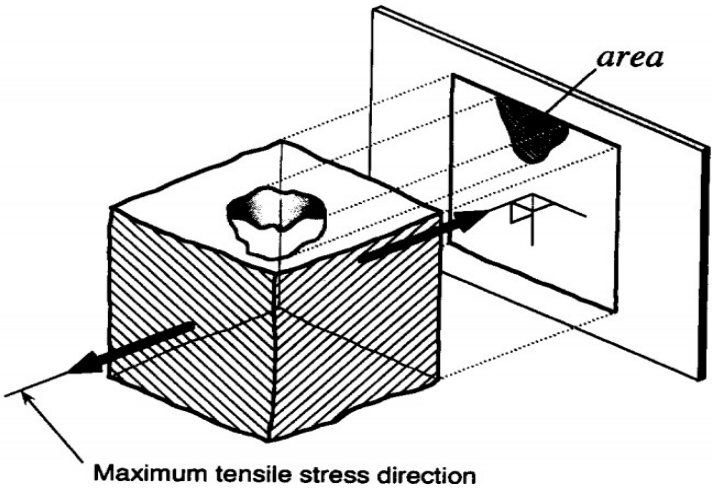

Figure 2.1– Definition of the $\sqrt{area}$ parameter (Murakami and Endo, 1994).

projection of the defect onto the plane perpendicular to the maximum principal stress, as illustrated in Fig. 2.1. Furthermore, the maximum value of the stress intensity factor along the front of various surface cracks was determined by three-dimensional numerical elastic analysis, and it was correlated with the crack area by the following formula:

$$K = 0.65\sigma_0\sqrt{\pi\sqrt{area}} \tag{2.2}$$

where K is the maximum stress intensity factor along the crack front, σ_0 is the remote stress applied to the surface crack and $\sqrt{area}$ is the square root of the crack area. From Eq. (2.2), the stress intensity factor range under fully reversed loading can be written as

$$\Delta K = 0.65\Delta\sigma_0\sqrt{\pi\sqrt{area}} \tag{2.3}$$

where $\Delta\sigma_0$ is the stress range applied to the defect.

To evaluate the right side of Eq. (2.1), the following relation between ΔK_{th} and $\sqrt{area}$ was derived by fitting test data of various defects and cracks:

$$\Delta K_{\mathrm{th}} = 3.3 \times 10^{-3}(H_{\mathrm{v}} + 120)(\sqrt{area})^{\frac{1}{3}} \tag{2.4}$$

where H_{v} is the Vickers hardness of the material. Substituting Eq. (2.3) and Eq. (2.4) into Eq. (2.1), the following formula for fatigue limit prediction was obtained:

$$\sigma_{\mathrm{w}} = \frac{1.43(H_{\mathrm{v}} + 120)}{(\sqrt{area})^{\frac{1}{6}}} \tag{2.5}$$

where the unit of σ_{w} is MPa, that of H_{v} is kgf/mm^2, and that of the $\sqrt{area}$ is μm. The accuracy of Eq. (2.5) in estimating the fatigue limit of various types of defects and metallic materials is mostly less than 10%, for $\sqrt{area}$ less than 1000 μm and H_{v} ranging from 70 to 720 kgf/mm^2 (Murakami and Endo, 1994). Note that the Murakami–Endo model is often called the $\sqrt{area}$ parameter model since $\sqrt{area}$ is judged to be the proper geometrical parameter for estimating the influence of a defect on the fatigue limit.

2.2 New critical plane criterion

Castro et al. (2019) used the formulation of Murakami and Endo (1986) as a starting point to develop a critical plane criterion for the fatigue limit of metals containing small defects. The idea is to compare a normal stress-based fatigue parameter associated with a given plane with the uniaxial fatigue strength expressed in terms of $\sqrt{area}$.

To formulate the fatigue criterion, consider a material volume containing a small defect together with an x-y-z coordinate system located at the free surface, as shown in Fig. 2.2. A new x'-y'-z' coordinate system can be obtained from the original one by rotating the coordinate axes through an angle θ about the z axis. The two normal stresses associated with the θ-oriented coordinate system are denoted by $\sigma_{\mathrm{x}'}(\theta, t)$ and $\sigma_{\mathrm{y}'}(\theta, t)$, where t is the time. The linear combination of these normal stresses is written as

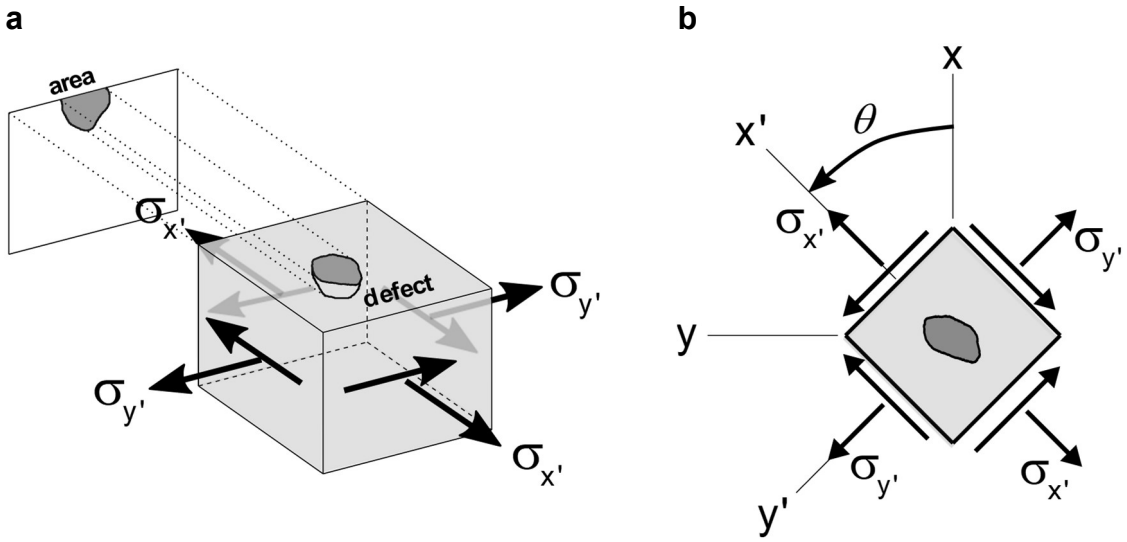

Figure 2.2 – (a) Material volume with a small defect and (b) definition of a θ-oriented x'- y'- z' coordinate system.

$$\Sigma = \sigma_{x'} + k\sigma_{y'} \tag{2.6}$$

where k is a constant associated with the stress biaxiality effect. The fatigue limit criterion then takes the following form:

$$\mathrm{FP} = \Sigma_a^m \langle \Sigma_{max} \rangle^{1-m} \leq \sigma_{w'} \tag{2.7}$$

where FP is the 'fatigue damage driving parameter.' The subscripts a and max stand for the amplitude and the maximum value of Σ, respectively. The symbol m is a material constant. The quantity $\sigma_{w'}$ is the uniaxial fatigue strength expressed in terms of $\sqrt{area}$, the square root of the area obtained by projecting the defect onto the plane perpendicular to the x′ direction. To ensure that the fatigue parameter is zero whenever the maximum value of Σ is negative, Macaulay brackets ⟨ ⟩ defined as $\langle x \rangle = 0.5(x + |x|)$ are used. Note that both the fatigue parameter, FP, and the fatigue strength, $\sigma_{w'}$, can vary with the plane. Therefore, the critical plane is defined as the plane on which the fatigue parameter relative to the fatigue strength attains its maximum, i.e., the plane on which the quantity $\mathrm{FP} - \sigma_{w'}$ is maximum.

The fatigue limit model in Eq. (2.7) can be interpreted as follows. A 'safe condition' is predicted to occur if the fatigue parameter is less than the fatigue strength, i.e. FP $< \sigma_{w'}$. If FP $> \sigma_{w'}$, fatigue failure is predicted to occur. The equality FP $= \sigma_{w'}$ corresponds to the fatigue limit condition.

An important component of Eq. (2.7) is the Walker relation (Walker, 1970; Dowling et al., 2009). It is used to improve the fatigue limit estimates for stress histories with mean stresses. In the study by Castro et al. (2019), it was shown that the estimates yielded by the Walker relation for carbon steel test data were significantly improved when compared with the ones provided by the Smith−Watson−Topper relation ($m = 0.5$). The expression $m = 0.806 - 3.465 \times 10^{-4}\, H_v$ was also derived by Castro et al. (2019) for steels.

Another feature of the model is that the fatigue parameter is sensitive to the normal stress $\sigma_{y'}$ parallel to the plane containing the projected defect. This allows describing the biaxial stress effect (Murakami and Takahashi, 1998; Beretta and Murakami, 2000). To illustrate this effect, Fig. 2.3 shows a specimen with a small hole tested under fully reversed axial stress at the fatigue limit, and another specimen tested under fully reversed torsional loading at the fatigue limit. In the first case, the critical plane occurs at $\theta = 0^o$, where $\Sigma_a = \Sigma_{max} = \sigma_w$, and the fatigue parameter FP $= \sigma_w$. In the second case, the critical planes occur at $\theta = 45^o$ and 135^o, where $\Sigma_a = \Sigma_{max} = (1-k)\tau_w$ and the fatigue parameter is FP $= (1-k)\tau_w$. Equating these two fatigue parameters, the following expression is obtained:

$$k = 1 - \frac{\sigma_w}{\tau_w} \tag{2.8}$$

The typical value of k is −0.18, as the average value of the τ_w/σ_w ratio is 0.85 according to the fatigue limits reported by Beretta and Murakami (2000).

A distinguishing feature of the proposed critical plane criterion is that, for each plane perpendicular to a given x′ direction described by an angle θ, the fatigue parameter at that plane, FP(θ), is compared with the uniaxial fatigue strength $\sigma_{w'} = \sigma_w(\sqrt{area(\theta)})$, in which the area is

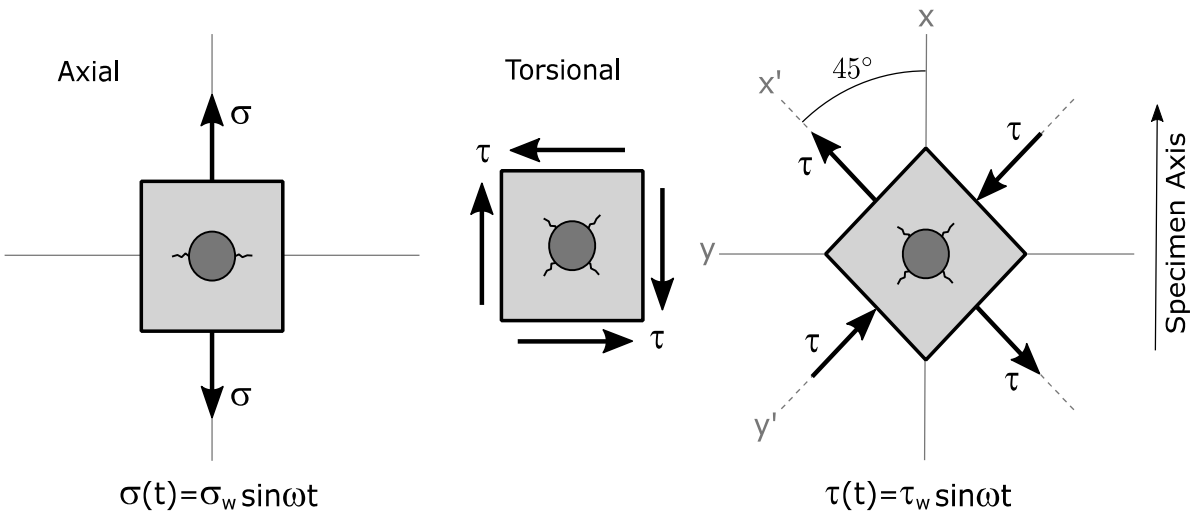

Figure 2.3 – Schematic of the biaxial stress effect for a material volume with a small defect.

obtained by projecting the defect onto the plane perpendicular to the x′ direction. Therefore, the criterion incorporates the possibility that the fatigue strength of a material volume containing an irregularly shaped defect may vary with the plane.

3 Fatigue experiments

The material used in this study is 304L austenitic stainless steel. The chemical composition of the material in weight percentage is 0.02 C, 18.16 Cr, 8.30 Ni, 1.34 Mn, 0.43 Si, 0.43 Si, 0.25 Cu, 0.22 Mo, 0.08 N, 0.03 P, 0.03 S, and Fe as balance. The material was acquired as extruded cylindrical bars with a diameter of 19.05 mm. To relieve residual stresses due to the extrusion process, the bars were normalized at 1050 ºC for 1 h. Figure 3.1 shows the microstructure of the material after heat treatment. The extrusion (axial), radial and tangential directions are represented by the letters A, R, and T, respectively. The average grain size was measured by the Mean Lineal Intercept Procedure according to the ASTM E112 standard (2013). The material has an average grain size of 43 µm on the plane perpendicular to the extrusion direction, and of 46 µm on the other planes (Bemfica et al, 2019).

The mechanical properties of the 304L stainless steel were determined in a previous work by Carneiro Junior (2017) and are listed in Table 3.1. This table also includes the Vickers hardness of the material, which was measured in the present work using a ZwickRoell ZHU 250 hardness testing machine and following the ASTM E92 standard (2017).

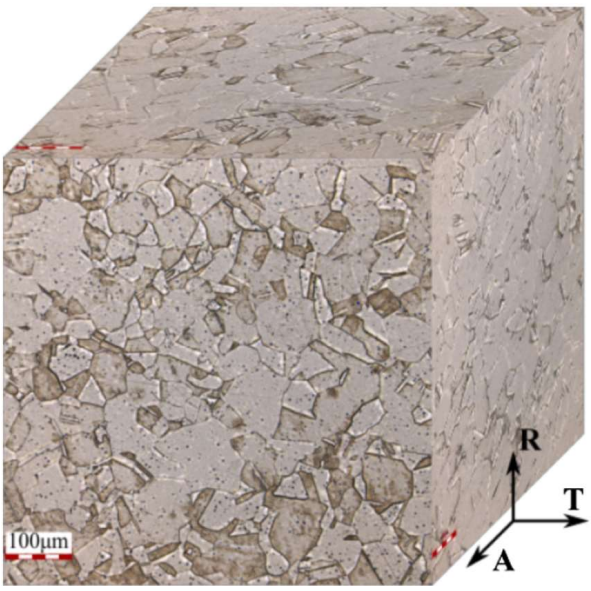

Figure 3.1 – Microstructure of the 304L stainless steel.

Table 3.1 – Mechanical properties of the 304L stainless steel

Young's modulus	208 GPa
0.2%-offset yield stress	213 MPa
Ultimate tensile strength	616 MPa
Reduction in area	80%
Vickers hardness	160 kgf/mm²

Cylindrical solid specimens with the geometry and dimensions shown in Fig. 3.2 were produced according to the ASTM E466 standard (2015). The surface of each specimen was ground using sandpapers with grit numbers ranging from 220 to 2500. The surface roughness R_a was measured using an Olympus LEXT OLS4100 3D confocal laser microscope. The roughness of the surface was less than 0.1 μm, complying with the maximum surface roughness of 0.2 μm specified in the ASTM E466 standard (2015). After grinding, a cylindrical small hole was produced at the center of each specimen with a 400 μm end mill by using a Vega Model MVU920 Vertical Machining Center. The shape and dimensions of the milled holes were checked with the confocal laser microscope. An average of 452 μm in diameter and 354 μm in height was observed in the specimen holes, with little deviation (less than 5%) from the target $\sqrt{area}$ value of 400 μm.

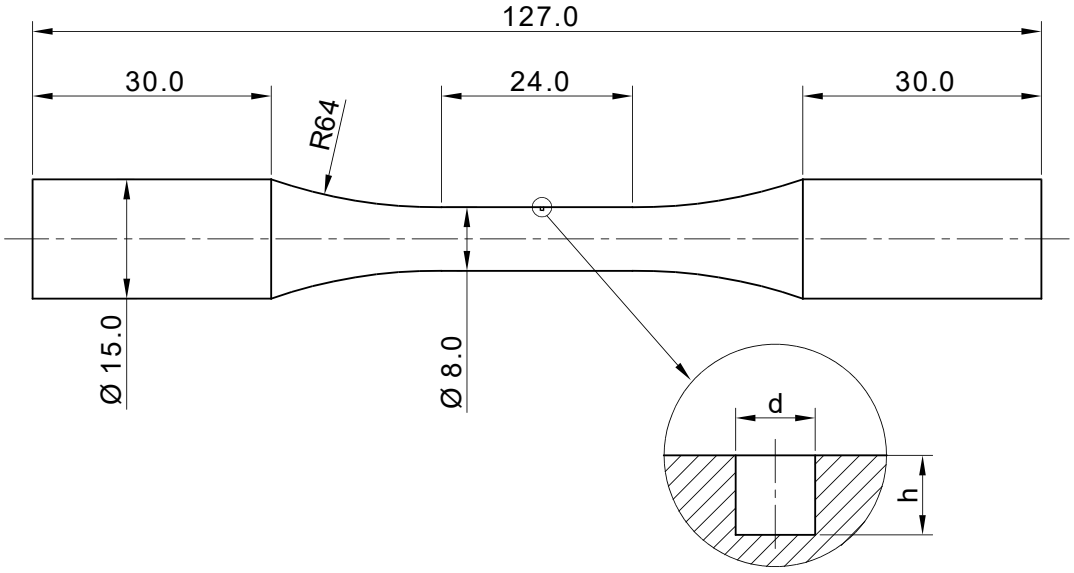

Figure 3.2 – Geometries of the specimen and defect (dimensions in mm).

The fatigue tests were conducted under force/torque-controlled loading at room temperature. Five types of fully reversed loading histories were considered: tension-compression, torsional, in-phase, 90º out-of-phase, and square-shape. The tension-compression tests were performed on an MTS 810 servo-hydraulic test system with an axial force capacity of 100 kN, while the torsional and axial-torsional tests were carried out on an MTS 809 servo-hydraulic test system whose capacity is 100 kN for axial force and 1100 Nm for torque. The ratio of shear stress amplitude to axial stress amplitude, τ_a/σ_a, was chosen to be 0.5 in the in-phase tests and 1 in both 90º out-of-phase and square-shape tests.

The loading paths corresponding to the five stress histories studied are depicted in a σ–τ stress space in Fig. 3.3. Fatigue tests were carried out until the total fracture of the specimen into two parts or were interrupted at 2×10^6 cycles (run-out condition). Loading frequencies ranged from 1 Hz to 12 Hz to avoid self-heating of the material. The fatigue limit was defined as the maximum stress amplitude at which run out occurred.

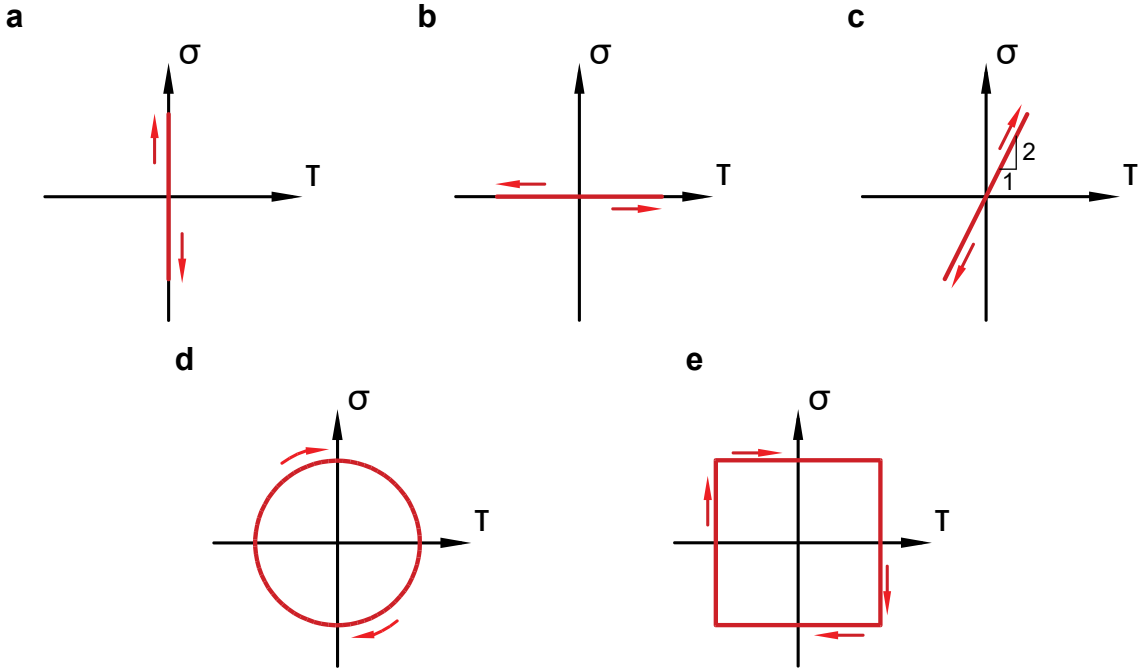

Figure 3.3 – Stress paths used in the fatigue tests: (a) axial, (b) torsional, (c) in-phase, (d) 90° out-of-phase, and (e) square-shape.

One tension-compression fatigue test was carried out until 10^7 cycles to check for the presence of non-propagating cracks in the vicinity of the defect. The other tests were not continued beyond 2 × 10^6 cycles since the low frequencies used would result in long test duration.

Each defect was inspected with a confocal laser microscope to measure the crack orientation at or just above the fatigue limit. The crack angle, θ, was defined according to the coordinate system described in Fig. 2.2, with the x-axis parallel to the specimen axis. The fracture surface of the specimens was analyzed using a scanning electron microscope (SEM).

The fatigue test results are summarized in Table 3.2. For each loading type, a series of fatigue tests were conducted in a stepwise manner to identify the threshold level at which run out occurred. A step of 10 MPa in the axial stress amplitude was chosen in the axial and axial-torsional tests. Likewise, a step of 10 MPa in the shear stress amplitude was adopted for the torsion tests. The specimens were identified by letters and sequential numbers. The letters represent the type of loading: U for uniaxial, T for torsional, I for in-phase, N for 90º out-of-phase and S for square-shape.

For tension-compression and torsional loadings, the observed fatigue limits were 170 MPa and 145 MPa, respectively. The ratio between the torsional and axial fatigue limits (τ_w/σ_w) of the 304L stainless steel was 0.85. This indicates an effect of the stress biaxiality on the torsional fatigue limit of 304L stainless steel containing a small defect. The crack angle was 0º for tension-compression and 45º/135º for torsion loading.

The observed fatigue limit for in-phase loading was $\sigma_a = 140$ MPa and $\tau_a = 70$ MPa and the crack angles were 20º. For 90º out-of-phase loading, the observed fatigue limit was $\sigma_a = \tau_a = 130$ MPa and the crack angles were 19º and 132º. For square-shape loading, the fatigue limit was $\sigma_a = \tau_a = 95$ MPa and the crack angle was 147º.

Table 3.2 – Fatigue test data of 304L stainless steel with a cylindrical defect of $\sqrt{area} = 400\ \mu$m.

Loading type	Specimen ID	σ_a [MPa]	τ_a [MPa]	θ [º]	N_f [cycles]	Note
Tension-compression	U02	180	–	0	111,364	Failure from defect
	U05	180	–	0	283,909	Failure from defect
	U04	170	–	–	–	Run out at 10^7 cycles
	U03	160	–	–	–	Run out at 2×10^6 cycles
Torsion	T03	–	155	45 / 135	498,575	Failure from defect
	T04	–	145	–	–	Run out at 2×10^6 cycles
	T02	–	135	–	–	Run out at 2×10^6 cycles
	T01	–	124	–	–	Run out at 2×10^6 cycles
In-phase	I02	150	75	20	620,247	Failure from defect
	I03	140	70	–	–	Run out at 2×10^6 cycles
	I01	130	65	–	–	Run out at 2×10^6 cycles
90º out-of-phase	N01	140	140	19 / 132	372,427	Failure from defect
	N03	130	130	–	–	Run out at 2×10^6 cycles
	N02	120	120	–	–	Run out at 2×10^6 cycles
Square-shape	S01	105	105	147	563,784	Failure from defect
	S02	95	95	–	–	Run out at 2×10^6 cycles

4 Results and discussion

4.1 Observation of surface fatigue cracks

The cracking behavior of the 304L stainless steel is examined in this section. In all tests stopped at the run-out condition of 2×10^6 cycles, no crack was observed in the vicinity of the defect. To check if non-propagating cracks might be formed after 2×10^6 cycles, specimen U04 was tested up to 10^7 cycles. No crack was found in the vicinity of the defect of this specimen, as shown in Fig. 4.1. The other tests were not continued beyond 2×10^6 cycles as the low loading frequencies used would result in long test duration. The absence of non-propagating cracks suggests that the threshold condition for crack initiation, instead of crack propagation, determines the fatigue limit of 304L stainless steel containing the defect type investigated. This means that if a crack is initiated in the defect, it will continue to propagate until failure. The absence of non-propagating cracks in the 304L stainless steel containing a small defect agrees with the observations by Ogura and Miyoshi (1986) on a sharp notch made of similar material.

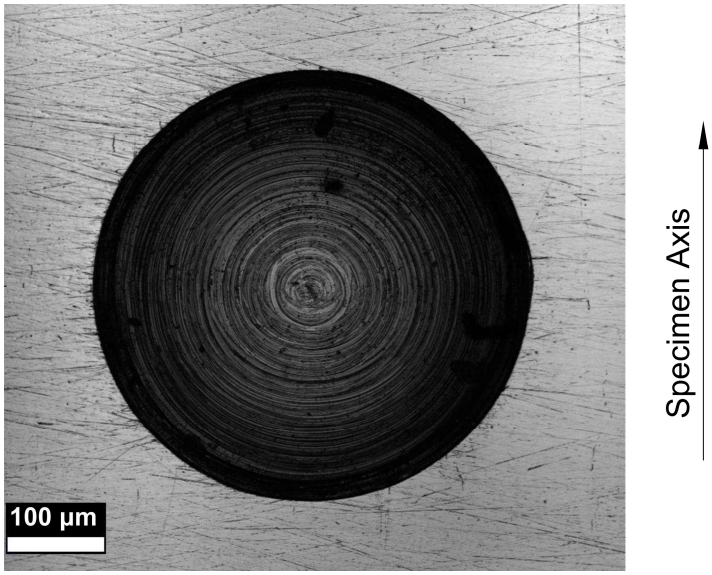

Figure 4.1 – Defect of the specimen U04 after 10^7 loading cycles. Test conducted under tension-compression loading at $\sigma_a = 170$ MPa.

The present study indicates that the fatigue limit of 304L stainless steel containing a hole of $\sqrt{area} = 400\ \mu$m is related to crack initiation, instead of crack propagation. The work conducted by Schönbauer et al. (2017b) on stainless steel 17-4PH (AISI 630) pointed to similar observations. These authors observed non-propagating cracks at the edge of holes with diameters of 50 μm, but for holes larger than 100 and 300 μm in diameter, crack initiation was not observed at the fatigue limit. In their study, one test was performed slightly below the fatigue limit and another at a stress amplitude 3% higher than the fatigue limit. Crack initiation was not observed after 1.5×10^7 cycles in the first test, while in the second a crack initiated in the defect before 1.5×10^5 cycles and propagated until final failure. They concluded that for holes larger than certain sizes, the fatigue limit can be defined as the stress amplitude at which a crack will or will not initiate at the hole edges.

The cracks observed in the tests performed with stress amplitudes just above the fatigue limit are presented in what follows. The examination of these cracks will serve to identify the cracking behavior of the material and, later in this chapter, the crack angles will be compared with the critical plane orientations yielded by the fatigue criterion presented in Section 2.2.

Figure 4.2 shows the crack formed in the defect of the specimen U02, which was tested under tension-compression loading at $\sigma_a = 180$ MPa (N_f = 111,364 cycles). Referring to the coordinate system in Fig. 2.2, the crack angle was 0º. The specimen U05 was tested at the same stress amplitude of 180 MPa (N_f = 284,909 cycles) to monitor the crack growth in the vicinity of the defect. The loading frequency ranged from 1.5 to 3.0 Hz to keep up with the growth of the crack. After 80,044 cycles a crack of 89 µm length was observed at the right side of the defect. From 100,144 to 160,144 cycles, crack length was measured every 10,000 cycles. The measured lengths in microns were: 220, 301, 429, 486, 543, 612 and 702. After 234,177 cycles, a new crack 327 µm long was observed at the left side of the defect, while the one on the right side was already 1185 µm long. The small crack that initiated at the right side of the hole propagated for about 70% of the total life.

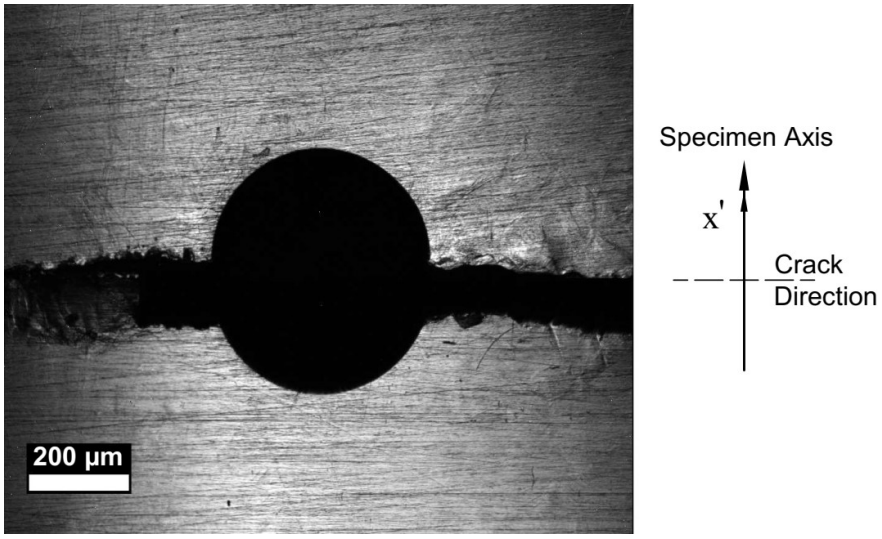

Figure 4.2 – Crack observed on the specimen U02 tested under tension-compression loading (σ_a = 180 MPa, N_f = 111,364 cycles).

Figure 4.3 shows the cracks observed after 236,412 cycles in the defect of the specimen T03 tested under torsional loading ($\tau_a = 155$ MPa, $N_f = 498{,}575$ cycles). Crack initiation occurred both at the edge of the hole and the bottom of the defect, and the surface crack propagated in the plane perpendicular to the direction of the maximum principal stress. The observed crack angles were 45º and 135º. After 236,412 cycles, the lengths of the four surface cracks were in the range of 1009 to 1095 µm. Note that failure occurred at 498,575 cycles, which implies that small crack growth consumed a significant part of the total life (more than 53%).

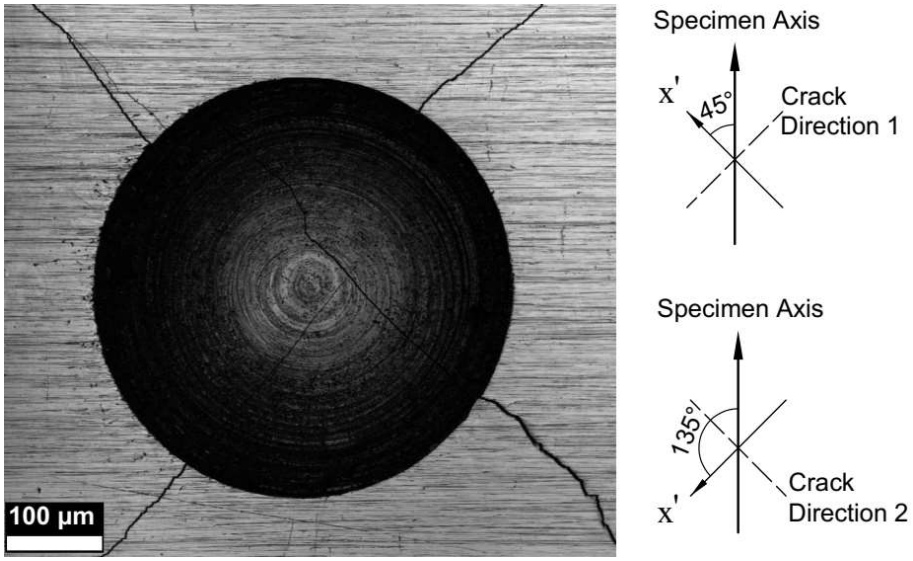

Figure 4.3 – Cracks observed on the specimen T03 tested under torsion loading (τ_a = 155 MPa, N_f = 498,575 cycles). Image taken at 236,412 cycles.

Figure 4.4 shows the crack observed after fracture of the specimen I02 tested under in-phase loading. The crack angle was 20º. For the specimen N01 tested under 90º out-of-phase loading, the crack observed after 322,465 cycles (N_f = 372,427 cycles) is shown in Fig. 4.5a. The critical plane angle was 132º. Another crack oriented at 19º was observed after the fracture of the specimen, as shown in Fig. 4.5b. The 132º-oriented crack was responsible for the fracture, while the 19º-oriented crack appeared on the surface in the last 49,962 cycles. Figure 4.6 shows the crack observed on the defect of the specimen S01, which was subjected to a square-shape loading and endured 563,784 cycles. The critical plane angle was 147º.

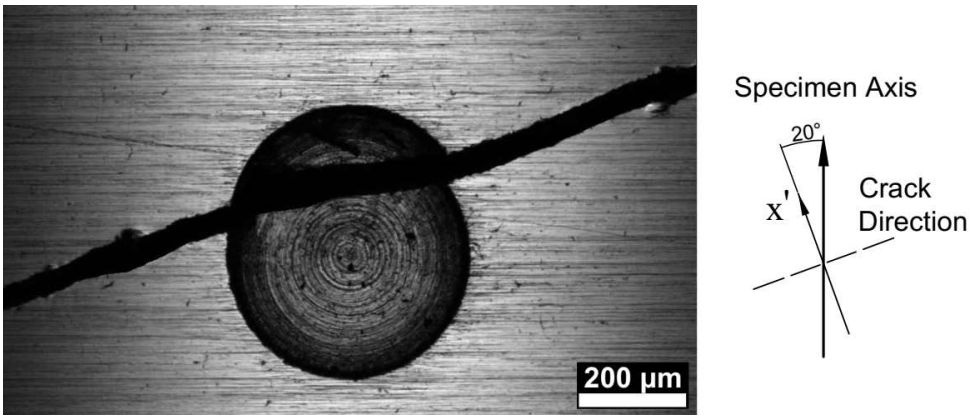

Figure 4.4 – Crack observed on the specimen I02 tested under in-phase loading (σ_a = 150 MPa, τ_a = 75 MPa, N_f = 620,247 cycles).

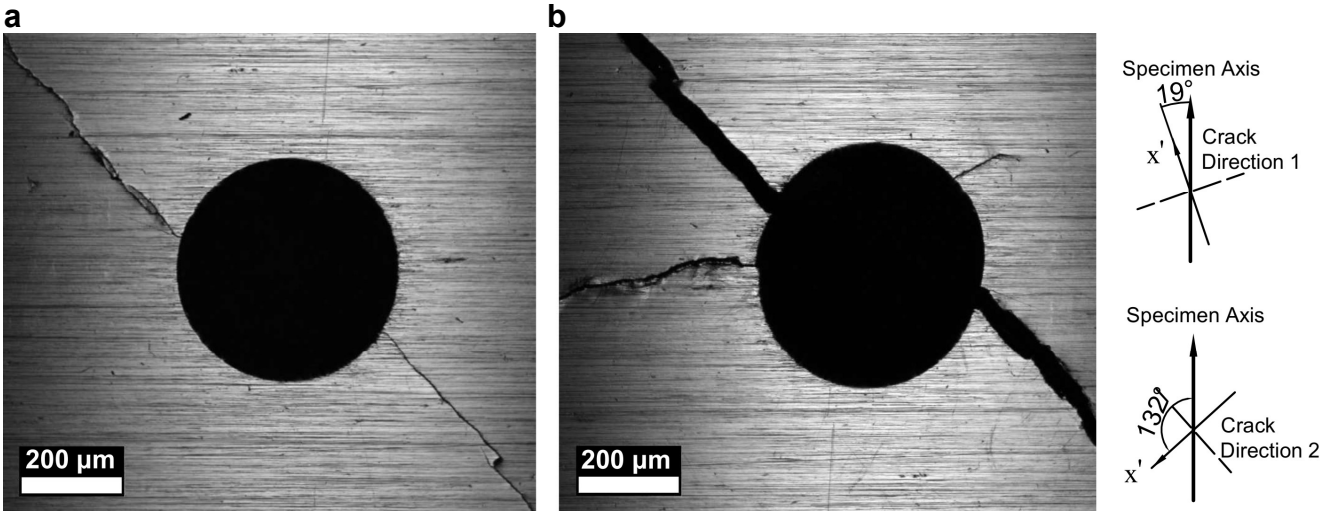

Figure 4.5 – Cracks observed on the specimen N01 tested under 90º out-of-phase loading (σ_a = τ_a = 140 MPa, N_f = 372,427 cycles): (a) image taken at 322,465 cycles, (b) image taken after fracture showing a secondary crack.

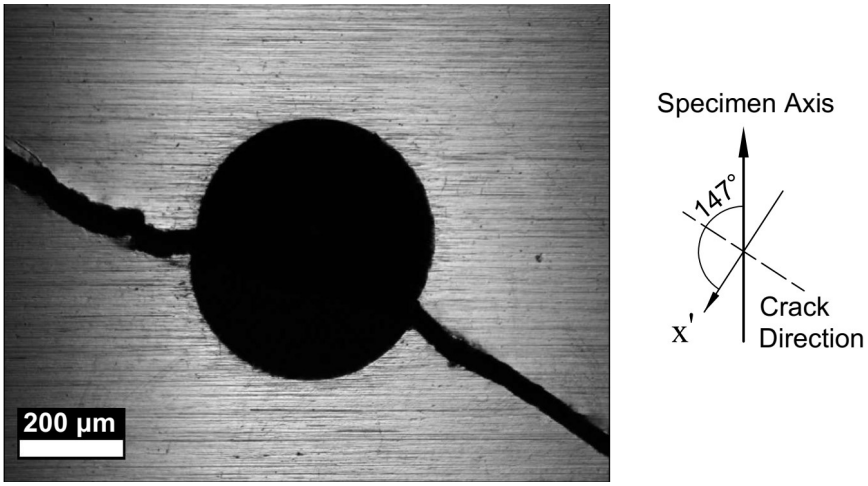

Figure 4.6 − Crack observed on the specimen S01 tested under square loading path ($\sigma_a = \tau_a = 105$ MPa, $N_f = 563{,}784$ cycles).

4.2 Observation of fracture surfaces

The fracture surfaces of the specimens were observed by scanning electron microscopy (SEM). Three distinct regions can be identified, as shown in Fig. 4.7 for the case of the specimen I02. In region A, crack initiation is followed by small crack growth around the defect. Fatigue crack growth occurred in the region B, in which the white arrows indicate the direction of marks that propagated from the defect to the region of fast fracture (region C).

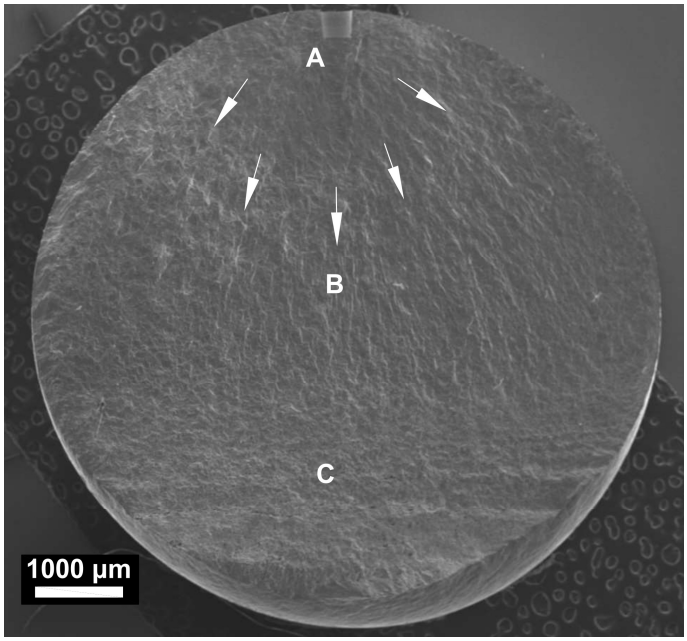

Figure 4.7 – SEM image of the fracture surface of the specimen I02.

The fracture surface near the defect of each specimen is shown in Fig. 4.8. The blue arrows indicate a relatively smooth area where cracks probably initiated, while the green arrows show secondary cracks. Note that the exact point where the cracks initiated are not easily identifiable, which means that the blue arrows provide an indication of the possible crack initiation sites. Figure 4.8a shows that in addition to the two cracks formed in the defect subjected to tension-compression, another crack propagated from the bottom of the defect. In the torsion test, the two cracks that initiated near the surface (blue arrows) and the crack that initiated on the other critical plane (green arrows) are shown in Fig. 4.8b. Figure 4.8c shows the cracks initiated on the sides of the defect in the in-phase test, and another crack that propagated from the bottom of the hole (green arrow). Figure 4.8d shows the cracks initiated close to the surface in the 90º out-of-phase test and also the crack on the other critical plane. In Fig. 4.8e, the blue arrows point to the sites where cracks were possibly formed in the defect subjected to the square loading path.

4.3 Fatigue limit prediction

The observed fatigue limits and the estimates yielded by the proposed fatigue criterion are compared in Table 4.1. The estimates were made using $k = -0.18$ in Eq. (2.8), since for the 304L stainless steel $\tau_w/\sigma_w = 0.85$. The uniaxial fatigue strength in the right side of Eq. (2.7) was evaluated using the Murakami–Endo formula given by Eq. (2.5). To calculate the percentage difference between the estimated and observed fatigue limits, the τ_w values were used for the torsional test and the σ_w values for the other loading types

Table 4.1 – Observed and estimated fatigue limits. Fatigue criterion calibrated with the Murakami–Endo formula.

Loading type	Estimated [MPa]		Observed [MPa]		Difference
	σ_w	τ_w	σ_w	τ_w	[%]
Tension-compression	148	–	170	–	-13
Torsion	–	125	–	145	-14
In-phase	119	59	140	70	-15
90º out-of-phase	116	116	130	130	-11
Square-shape	85	85	95	95	-11

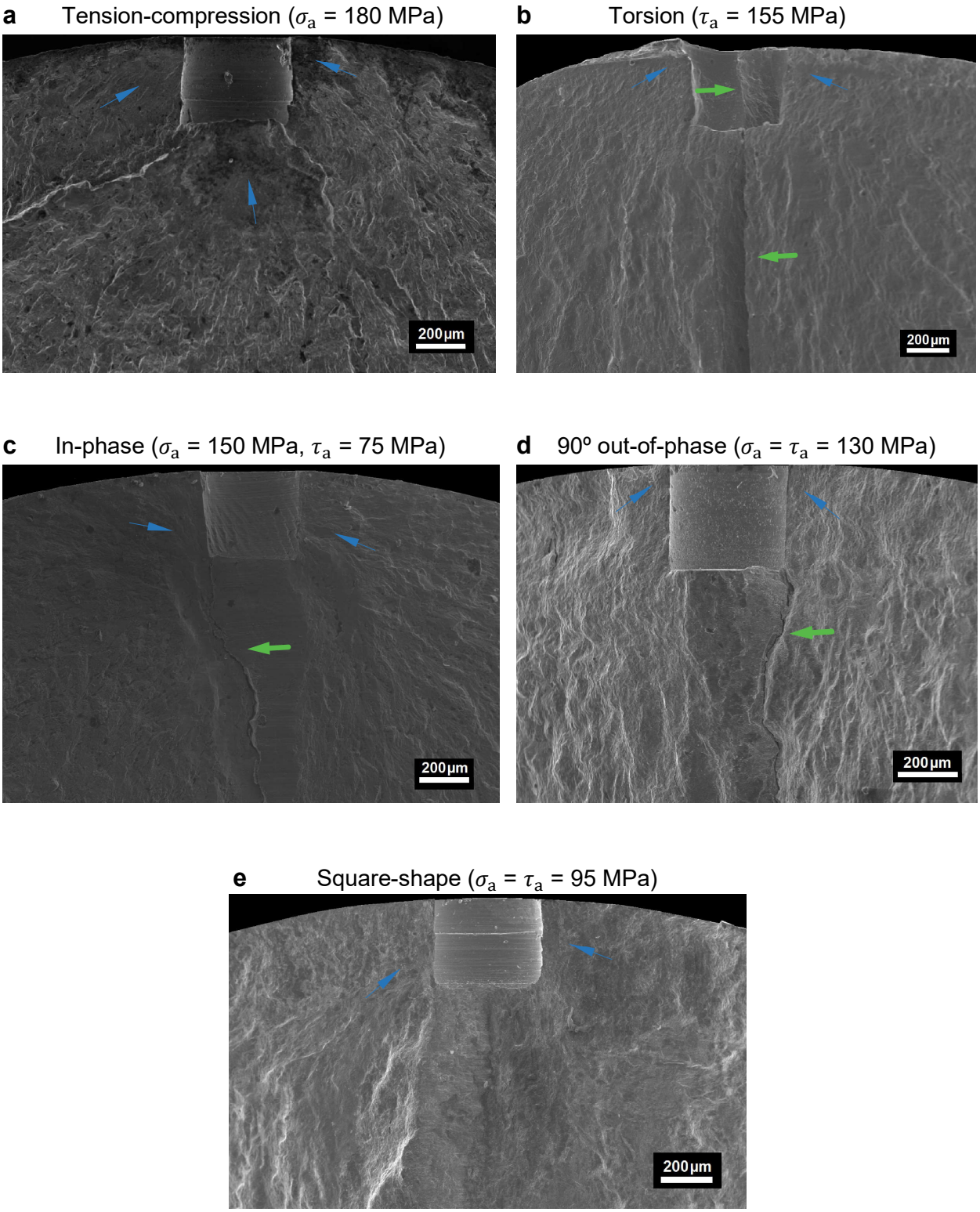

Figure 4.8 – SEM image of the fracture surface near the defect for the test subjected to: (a) tension-compression, (b) torsion, (c) in-phase, (d) 90º out-of-phase, and (e) square loading path.

As seen in Table 4.1, conservative estimates in the range of -15% to -11% were obtained for all loading types. This accuracy is similar to the results reported by Murakami and Endo (1986), in which the difference between estimated and observed uniaxial fatigue limits varied between -30.8% and -17.6% for two types of stainless steel, while for the other materials the difference was less than 10% in most cases.

Figure 4.9 presents the estimated and observed fatigue limits in a σ_a vs. τ_a diagram. The results for the in-phase and 90º out-of-phase loadings are compared in Fig. 4.9a, and those for the square loading path in Fig. 4.9b. As seen in Fig. 4.9a, the increase of the phase angle φ from 0º to 90º has a beneficial effect on the fatigue limit, which was correctly described by the fatigue criterion. This effect occurs because the 90º out-of-phase loading produces a lower and more evenly distributed fatigue damage around the critical plane, relative to an in-phase loading with the same axial and shear amplitudes. Note that the estimated fatigue limit curves for the in-phase and square-shape loadings in Figs. 4.9a and b, respectively, are identical since these two loading conditions yield identical fatigue parameters when the same loading amplitudes are used.

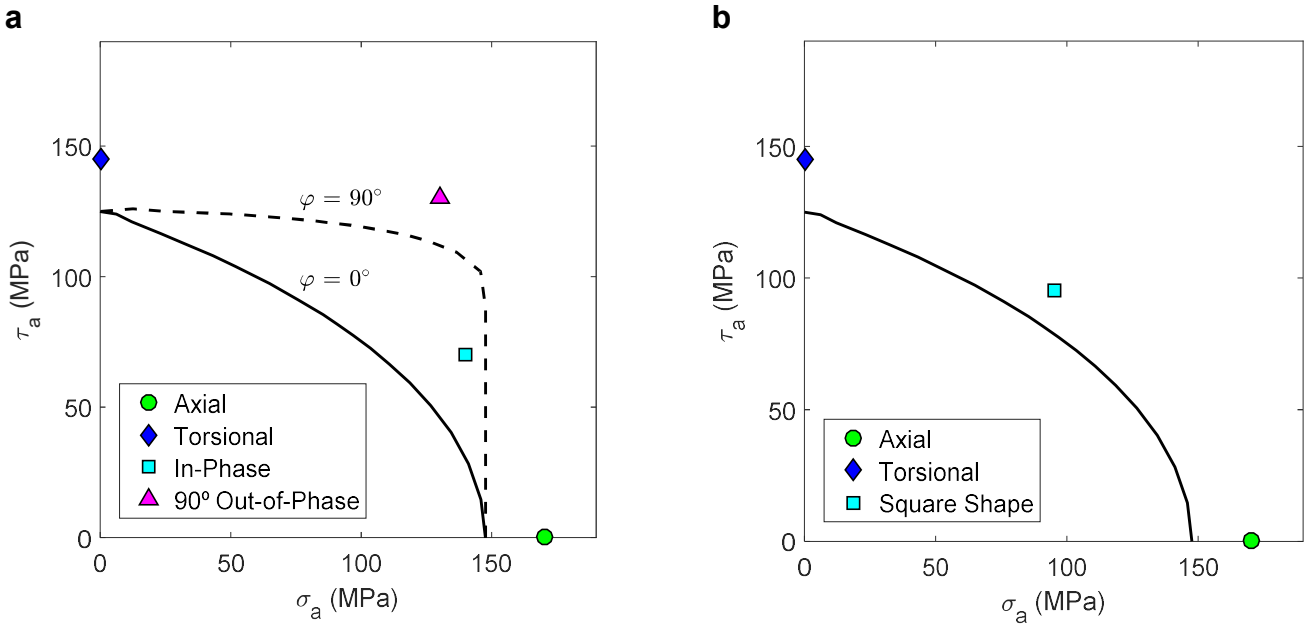

Figure 4.9 − Estimated and observed fatigue limits for (a) in-phase and 90º out-of-phase loadings and (b) square loading path. Fatigue criterion calibrated with the Murakami–Endo formula.

Table 2 presents the estimates yielded by the proposed fatigue criterion when the right side of Eq. (2.7) is evaluated using the observed uniaxial fatigue limit, instead of expressing it by the Murakami–Endo formula. The resulting fatigue limit estimates were within -2 to 3% relative to the observed values. One advantage of using the Murakami–Endo formula is that it can be used without performing any fatigue test. However, if more accurate estimates are needed when using the proposed fatigue criterion, one should calibrate it using observed fatigue limits, at least for the 304L stainless steel studied in the present work. Figure 4.9 presents the estimated and observed fatigue limits in a σ_a vs. τ_a diagram, showing that the good agreement between them.

Table 4.2 – Observed and estimated fatigue limits. Fatigue criterion calibrated with the observed uniaxial fatigue limit.

Loading type	Estimated [MPa]		Observed [MPa]		Difference
	σ_w	τ_w	σ_w	τ_w	[%]
Torsion	–	144	–	145	-1
In-Phase	137	68	140	70	-2
90º out-of-phase	134	134	130	130	+3
Square-shape	98	98	95	95	+3

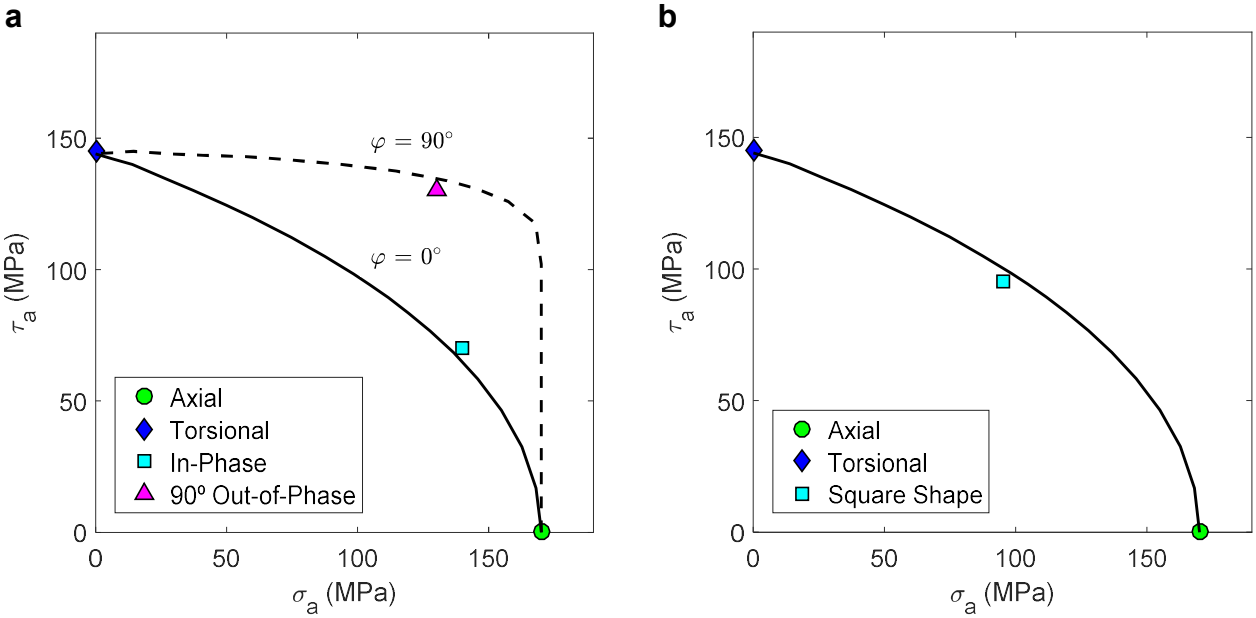

Figure 4.10 − Estimated and observed fatigue limits for (a) in-phase and 90º out-of-phase loadings and (b) share loading path. Fatigue criterion calibrated with the observed uniaxial fatigue limit.

4.4 Crack direction prediction

In addition to being able to predict fatigue strength well for a variety of loading conditions, a critical plane criterion should also be consistent with the physically observed damage (Socie and Bannantine, 1988; Jiang et al., 2007). In other words, it is desirable that the critical plane orientation estimated by the fatigue criterion agrees with the observed crack angles. In this section, this type of experimental evaluation is performed for the proposed critical plane model using the crack angles observed in the 304L stainless steel.

Figure 4.11 shows the observed crack angles and the fatigue parameter variation over the angle θ for each of the loading conditions. The fatigue parameter was normalized so that the maximum fatigue parameter is unity. The observed crack angles are represented by the vertical dashed lines. As discussed in Section 4.1, these angles were measured in the tests performed with stress amplitudes just above the fatigue limit. Note that for the cylindrical holes investigated, the right side of Eq. (2.7) is constant because the projected are does not vary with the plane. Therefore, the planes at which the fatigue parameter is maximum are those where fatigue cracks are expected to initiate. The estimated and observed crack angles are in excellent agreement for the tension-compression, torsional, in-phase, and square-shape loadings. For the test performed under 90º out-of-phase loading, the estimated crack angles of 38º and 142º were reasonably good compared with the observed angles of 19º and 132º. For the test conducted under square loading path, two critical planes were estimated at the angles of 32º and 148º, but only one crack oriented at 147º was observed.

The overall good agreement between estimated and observed crack angles suggests that the cracking behavior of 304L stainless steel containing a small defect is primarily governed by normal stresses (Mode I failure) for the range of lives investigated ($10^5 - 2 \times 10^6$ cycles).

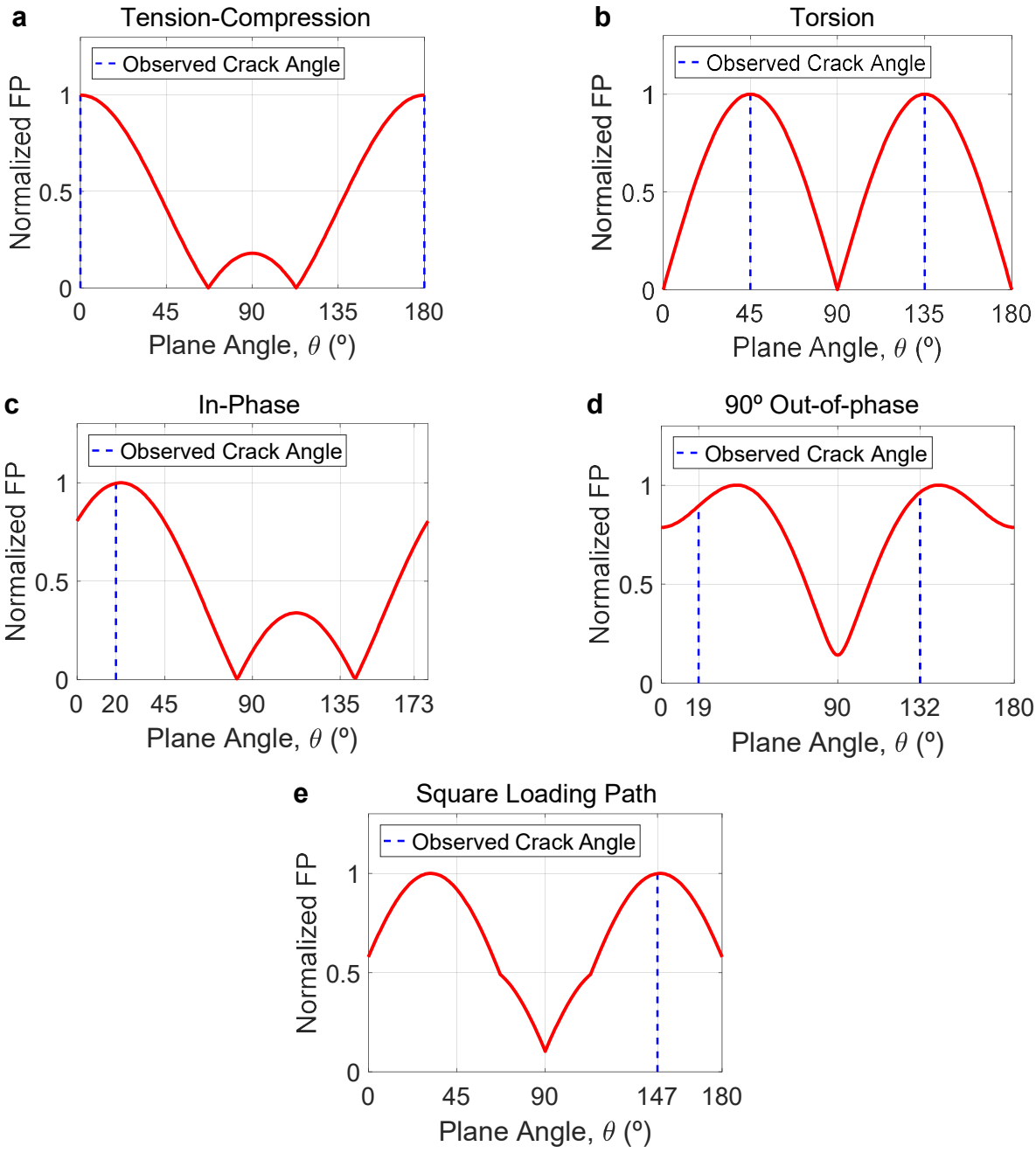

Figure 4.11 – Observed crack angles and fatigue parameter for the tests performed under (a) tension-compression, (b) torsion, (c) in-phase, (d) 90º out-of-phase, and (e) square loading path.

5 Conclusions and future work

5.1 Conclusions

A critical plane fatigue criterion developed by Castro et al. (2019) was evaluated considering new fatigue limit data of 304L stainless steel containing a cylindrical hole of $\sqrt{area} = 400$ μm. Fatigue tests were performed under fully reversed force/torque-controlled loading. Tension-compression, torsion, in-phase, 90º out-of-phase, and square-shape loading conditions were used in the tests. The main observations and conclusions can be summarized as follows:

(1) The ratio of torsional to axial fatigue limits was found to be 0.85. This indicates an effect of the stress biaxiality on the torsional fatigue limit of 304L stainless steel containing a small defect.

(2) In all tests, non-propagating cracks in the vicinity of the defect were not observed after 2×10^6 loading cycles (run-out condition). For the single tension-compression test conducted up to 10^7 loading cycles, non-propagating cracks were also not present in the defect. The absence of non-propagating cracks suggests that the threshold condition for crack initiation, instead of crack propagation, determines the fatigue limit of 304L stainless steel in the presence of the defect type investigated.

(3) The overall good agreement between estimated and observed crack angles suggests that the cracking behavior of 304L stainless steel containing a small defect is primarily governed by normal stresses (Mode I failure) for the range of lives investigated (10^5 –2×10^6 cycles).

(4) The determination of the constants of the fatigue criterion using the expression for the uniaxial fatigue strength developed by Murakami and Endo (1986) resulted in differences between estimated and observed fatigue limits within the range of -15 to 11%.

(5) The determination of the constants of the critical plane criterion using the experimentally measured uniaxial fatigue limit yielded fatigue limits differing -2 to 3% from the observed values.

5.2 Future work

The estimates yielded by the proposed critical plane fatigue criterion agreed with the test data well both for the fatigue limits and the crack directions. However, further examination of the fatigue criterion should be conducted for defects with different shapes, orientations, and sizes, and more complicated loading conditions. The possible extension of the fatigue criterion to life prediction of metals containing small defects is also a topic worthy of future investigation. Finally, the range of defect sizes for which the fatigue criterion is applicable should be better understood.

References

ASTM standard E112, 2013. Standard Test Methods for Determining Average Grain Size. ASTM International. West Conshohocken, PA.

ASTM standard E466, 2015. Standard Practice for Conducting Force Controlled Constant Amplitude Axial Fatigue Tests of Metallic Materials. ASTM International. West Conshohocken, PA.

ASTM standard E92, 2017. Standard Test Methods for Vickers Hardness and Knoop Hardness of Metallic Materials. West Conshohocken, PA.

Bemfica, C., Carneiro, L., Mamiya, E.N., Castro, F.C., 2019. Fatigue and cyclic plasticity of 304L stainless steel under axial-torsional loading at room temperature. International Journal of Fatigue 125, 249−361.

Bemfica, C., 2018. Fatigue and cyclic plasticity of 304L stainless steel under axial, torsional and proportional axial-torsional loading. MSc Dissertation. University of Brasilia.

Beretta, S., Blarasin, A., Endo, M., Giunti, T. and Murakami, Y., 1997. Defect tolerant design of automotive components. International Journal of Fatigue 19, 319–333.

Beretta, S. and Murakami, Y., 2000. SIF and threshold for small cracks at small notches under torsion. Fatigue and Fracture of Engineering Materials and Structures 23(1), 97−104.

Billaudeau, T., 2002. Fatigue multiaxiale des matériaux à défauts: mécanismes et critère d'endurance. Thèse, École doctorale des sciences pour l'ingénieur et aéronautique, Université de Poitiers

Billaudeau, T., Nadot, Y. and Bezine, G., 2004. Multiaxial fatigue limit for defective materials: mechanisms and experiments. Acta Materialia 52, 3911–3920.

Carneiro Junior, L. A., 2017. Estudo experimental da plasticidade cíclica e fadiga do aço inoxidável 304L. MSc Dissertation. University of Brasilia.

Castro, F.C., Mamiya, E.N., Bemfica, C., 2019. A critical plane model to multiaxial fatigue of metals containing small defects. Internal Report, Department of Mechanical Engineering, University of Brasilia.

Chaves, V., Beretta, G. and Navarro, A., 2017. Biaxial fatigue limits and crack directions for stainless steel specimens with circular holes. Engineering Fracture Mechanics 174(1), 139−154.

Chaves, V., Navarro, A. and Madrigal, C., 2015. Stage I crack directions under in-phase axial–torsion fatigue loading for AISI 304L stainless steel. International Journal of Fatigue 80, 10−21.

Dowling, N. E., 2013. Mechanical Behavior of Materials. Engineering Methods for Deformation,

Fracture, and Fatigue, vol. 4, 438−441.

Endo, M., 1999. Effects of small defects on the fatigue strength of steel and ductile iron under combined axial/torsional loading. Small fatigue cracks: mechanics, mechanisms and applications. Amsterdam: Elsevier, 375–387.

Endo, M. 2003. The multiaxial fatigue strength of specimens containing small defects. Biaxial/multiaxial fatigue fracture 31(1), 225–246.

Endo, M. and Ishimoto, I., 2006. The fatigue strength of steels containing small holes under out-of-phase combined loading. International Journal of Fatigue 28, 592–597.

Endo, M. and Ishimoto, I., 2007. Effects of phase difference and mean stress on the fatigue strength of small-hole-containing specimens subjected to combined load. Journal of Solid Mechanics and Materials Engineering 1, 343–354.

Endo, M. and Yanase, K., 2014. Effects of small defects, matrix structures and loading conditions on the fatigue strength of ductile cast irons. Theoretical and Applied Fracture Mechanics 69, 34–43.

Dowling, N.E., Calhoun, C.A. and Arcari, A., 2009. Mean stress effects in stress-life fatigue and the Walker equation. Fatigue and Fracture of Engineering Materials and Structures 32, 163–79.

Giglio, M., Beretta, S., Mariani, U. and Ratti, G. 2010. Defect tolerance assessment of a helicopter component subjected to multiaxial load. Engineering Fracture Mechanics 77, 2479–2490.

Groza, M., Nadot, Y., Varadi, K., 2018. Defect size map for nodular cast iron components with ellipsoidal surface defects based on the defect stress gradient approach. International Journal of Fatigue 112, 206–215.

Guerchais, R., Morel, F., Saintier, N. and Robert, C., 2015. Influence of the microstructure and voids on the high-cycle fatigue strength of 316L stainless steel under multiaxial loading. Fatigue & Fracture of Engineering Materials Structures 38(1), 1087–1104.

Karolczuk, A., Nadot, Y. and Dragon, A., 2008. Non-local stress gradient approach for multiaxial fatigue of defective material. Computational Materials Science 44, 464–475.

Lorenzino, P., Okazaki, S., Matsunaga, H. and Murakami, Y., 2015. Effect of small defect orientation on fatigue limit of carbon steels. Fatigue & Fracture of Engineering Materials & Structures 38, 1076–86.

Murakami, Y., 2019. Metal fatigue: Effects of small defects and nonmetallic inclusions. Second Edition. Elsevier.

Murakami, Y., 2012. Material defects as the basis of fatigue design. International Journal of Fatigue 41, 2−10.

Murakami, Y. and Endo, M., 1983. Quantitative evaluation of fatigue strength of metals containing various small defects or cracks. Engineering Fracture Mechanics 17(1), 1−15.

Murakami, Y. and Endo, M., 1986. Effects of Hardness and Crack Geometries on ΔK_{th} of Small Cracks Emanating from Small Defects. In: K.J. Miller, E.R. de Los Rios (Eds.), The Behavior of Short Fatigue Crack, Mechanical Engineering Publications 1(1), 275−293.

Murakami, Y. and Endo, M., 1994. Effects of defects, inclusions and inhomogeneities on fatigue strength. International Journal of Fatigue 16(3), 163−182.

Murakami, Y. and Nemat-Nasser, S., 1983. Growth and stability of interacting surface flaws of arbitrary shape. Engineering Fracture Mechanics 17(3), 193−210.

Murakami Y, Takahashi K., 1998. Torsional fatigue of a medium carbon steel containing an initial small surface crack introduced by tension-compression fatigue: crack branching, non-propagation and fatigue limit. Fatigue and Fracture of Engineering Materials and Structures 21, 1473–84.

Nadot, Y. and Denier, V., 2004. Fatigue failure of suspension arm: experimental analysis and multiaxial criterion. Engineering Failure Analyses 11, 485–499.

Nadot, Y. and Billaudeau, T., 2006. Multiaxial fatigue limit criterion for defective materials. Engineering Fracture Mechanics 73, 112–133.

Ogura, K. and Miyoshi, Y., 1986. Threshold behavior of small fatigue crack at notch root in type 304 stainless steel. Engineering Fracture Mechanics 25(1), 31−46.

Schönbauer, B. and Mayer, H., 2019. Effect of small defects on the fatigue strength of martensitic stainless steels. International Journal of Fatigue 127(1), 362−375.

Schönbauer, B., Yanase, K. and Endo, M., 2017a. Influences of small defects on torsional fatigue limit of 17-4PH stainless steel. International Journal of Fatigue 100(2), 540−548.

Schönbauer, B., Yanase, K. and Endo, M., 2017b. The influence of various types of small defects on the fatigue limit of precipitation-hardened 17-4PH stainless steel. Theoretical and Applied Fracture Mechanic 87(1), 35−49

Walker, K. 1970.The effect of stress ratio during crack propagation and fatigue for 2024-T3 and 7075-T6 aluminum. In: Effects of Environment and Complex Load History on Fatigue Life, ASTM STP 462. Am. Soc. for Testing and Materials, Philadelphia, PA, 1–14.